coatings

MDPI

Communication

Preparation, Microstructure, and Interface Quality of Cr_3C_2-NiCr Cladding Layer on the Surface of Q235 Steel

Wenyan Zhai [1,*], Jiajun Nan [1], Liang Sun [1,*], Yiran Wang [2] and Shiqing Wang [1]

[1] College of Materials Science and Engineering, Xi'an Shiyou University, Xi'an 710065, China
[2] State Key Laboratory for Mechanical Behavior of Materials, Xi'an Jiaotong University, Xi'an 710049, China
* Correspondence: 180606@xsyu.edu.cn (W.Z.); lsun@xsyu.edu.cn (L.S.)

Abstract: In this study, a Cr_3C_2-NiCr cermet cladding layer was prepared on the surface of Q235 steel via a high-speed laser cladding method. The effects of laser power, scanning speed, and overlap rate on the microstructure, cladding quality, and interfacial elements diffusion of Cr_3C_2-NiCr/Q235 steel were studied. The results show that there was an obvious transition layer at the interface of the Cr_3C_2-NiCr cladding layer and Q235 steel, indicating that the Cr_3C_2-NiCr cladding layer had an adequate metallurgical bond with the matrix. Fe, Cr, and Ni were diffused distinctly between the cladding layer and the matrix. The height and width of the Cr_3C_2-NiCr cladding layer increased, while the dilution rate decreased with the increase in the laser power. The maximum thickness of the transition layer was about 50 μm for the 6 mm/s sample, the weld heat affected zone was smaller, and it was shown that the productivity can be effectively improved. The sample with a 40% overlap rate exhibited the best flatness. The optimal laser power, scanning speed, and overlap rate of the Cr_3C_2-NiCr/Q235 steel were 1500 W, 6 mm/s, and 40%, respectively.

Keywords: Cr_3C_2-NiCr cermet; cladding layer; microstructure; interface

check for updates

Citation: Zhai, W.; Nan, J.; Sun, L.; Wang, Y.; Wang, S. Preparation, Microstructure, and Interface Quality of Cr_3C_2-NiCr Cladding Layer on the Surface of Q235 Steel. *Coatings* **2023**, *13*, 676. https://doi.org/10.3390/coatings13040676

Academic Editor: Cecilia Bartuli

Received: 27 February 2023
Revised: 22 March 2023
Accepted: 23 March 2023
Published: 26 March 2023

1. Introduction

The laser cladding method has been widely used in the field of surface modification due to its low dilution rate and the excellent metallurgical bond with the matrix it can help produce [1]. The wear and corrosion resistance of the metal matrix can be obviously increased by laser cladding, and this has attracted widespread attention [2]. During the preparation and application process, the cladding layer and the metal matrix provide reasonable hardness and toughness; therefore, researchers in recent years have studied some surfacing materials with high hardness, such as carbides, borides, and oxides of the metals, as the laser cladding layer [3–9]. However, the single hard phase forms poor metallurgical bonding with the matrix, which limits its industrial application during the process of laser cladding. The cermet materials simultaneously possess the unique properties of metals (high ductility, toughness, and thermal conductivity) and ceramics (high melting point, hardness, and wear resistance). Therefore, the research scholars are focused on the cermet cladding layer [10–12].

Cr_3C_2-NiCr retains good oxidation resistance at high temperature, due to the dense and stable Cr_2O_3 layer [13]. Cr_3C_2 particles are usually decomposed into other carbides, such as Cr_7C_3 and $Cr_{23}C_6$, before solidification [14,15]. Since the melting point and hardness of Cr_7C_3 and $Cr_{23}C_6$ are both lower than Cr_3C_2, the wear resistance of Cr_7C_3 processed by a laser is lower than that of Cr_3C_2 in high wear resistance applications [16–20]. Generally, NiCr is added to Cr_3C_2 via an in-situ synthesis method. The Cr_3C_2-NiCr cermet coating is prepared by wrapping Cr_3C_2 with NiCr, which greatly improves the mechanical properties of the material. The hardness of the Cr_3C_2 hard phase and the toughness of the NiCr adhesive phase are both improved [21].

Studies on laser cladding Cr_3C_2 matrix composites have mainly focused on the characterization of microstructure and phase composition, and the evaluation of wear or corrosion behavior [22–28]. Few studies have focused on the role of processing variables, such as energy input and scanning speed. R. A. Rahman Rashid et al. conducted some research on laser processing parameters, and the conclusions were of great significance. R. A. Rahman Rashid et al. [29] prepared the laser cladding layer using 316L stainless steel on mild steel and studied the significant variation in the clad thickness, the depth of penetration of the melt pool, and the depth of the heat affected zone (HAZ). They observed and correlated with the process parameters including laser power, scan speed, dilution, and the specific energy of the laser beam. C. Barr et al. [30] studied the low cycle fatigue behavior of 300 M steel by laser directed energy deposition repair. R. A. Rahman Rashid et al. [31] studied LPHT treatment, which can be effectively employed for localized control of the microstructure in the laser clad-repaired parts by tuning the laser reheat parameters. G. X. Li et al. [32] studied the influence of machining parameters on the machinability of selective laser melted (SLMed) Ti6Al4V tubes, including cutting forces, machined surface roughness, and tool wear at varying cutting parameters.

Therefore, the processing parameters of laser cladding were worth studying for Cr_3C_2-NiCr cermet cladding layer. L. Venkatesh et al. [24] studied the relative hardness of the laser clad layers, which was observed to drop with an increase in laser power, and the wear resistance of the coating was improved. J. Morimoto [25] studied the melt depth of Cr_3C_2-25%NiCr and Ni-Cr sprayed coatings, which was increased by raising the power of a direct diode laser, and the wear resistance of the coating was also improved. L. Venkatesh et al. [33] studied the carbide content of laser clad layers. It was decreased with increasing laser power owing to the increased dilution from the substrate. The cooling rate determined by the laser beam scan speed had an additional effect in reducing the carbide content in laser clad layers. Lou et al. [21] studied the microstructure and formation mechanism of a laser cladding cermet layer, and they found that the laser scanning velocity had a significant effect on carbide content. The solidification rate of the metal molten pool increased, while the size of carbides decreased with the increase in the scanning speed. With the increase in carbide content, the content of Cr_3C_2 increased and the content of Cr_7C_3 decreased.

In the present study, the Cr_3C_2-NiCr cermet cladding layer was prepared on the surface of Q235 steel by a high-speed laser cladding method. The influences of laser power, scanning speed, and overlap rate on the microstructure and cladding quality of Cr_3C_2-NiCr/Q235 steel were studied. In addition, the interfacial quality and elements diffusion were also researched. The aim of this study was to explore the optimal laser cladding technological parameter of the Cr_3C_2-NiCr/Q235 steel.

2. Experimental

2.1. Materials

Q235 steel was used as the substrate material in this test; its chemical composition is shown in Table 1. The substrate material was polished with sandpaper before laser cladding, and then degreased with acetone. Commercial Cr_3C_2-25%NiCr cermet (Yinghe metal materials Co., LTD, Xingtai, Hebei province, China) powder was used as raw materials. The ratio of Ni and Cr was 4:1. The particle size of the powder was 10–50 µm, and the melting point was about 1800 °C. The powder was regular in shape (spherical or sphere-like) with excellent liquidity, as shown in Figure 1. NiCr is capable of reducing thermal stress, which is beneficial to obtaining free crack coatings. The Cr_3C_2-NiCr coating was hard and compact with low internal residual stress [34], which could be maintained below 1000 °C.

Table 1. Main chemical composition of Q235 steel (wt. %).

C	P	S	Mn	Si	Fe
0.17–0.24	≤0.03	≤0.03	0.35–0.65	0.17–0.37	Bal.

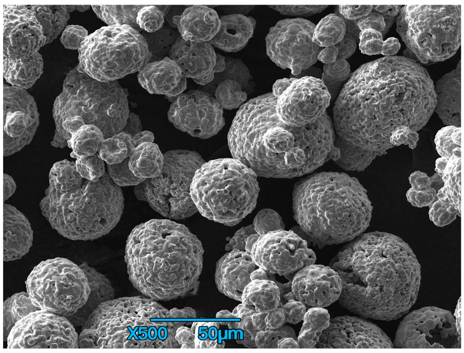

Figure 1. The morphology of the Cr_3C_2-NiCr powder.

2.2. Laser Cladding Process

A high-speed laser cladding machine was employed in this study with the nominal output power of 2000 W. Coaxial laser injection with argon auxiliary gas was used to protect the coating from oxidation. Paraxial powder feeding technology was adopted in the process of laser cladding. The angle between the powder outlet and the substrate surface was about 45°, and Figure 2 shows its schematic diagram. In this experiment, the influence of the output power, scanning speed, and overlap rate on the cladding quality was studied. The detailed laser cladding test parameters are shown in Tables 2–4. The distance between the laser head and the workpiece was 10 cm. The distance between the powder feed tube and the workpiece was 5 cm. The overlap between tracks was 40%–60%. The number of tracks and layers deposited were 20 and 1, respectively.

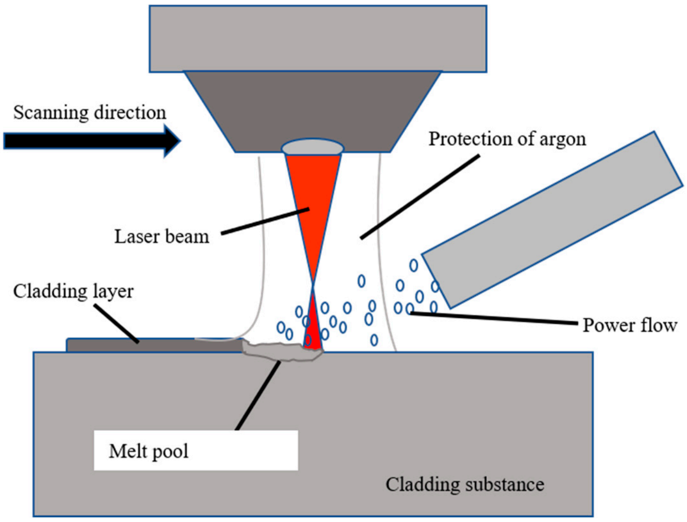

Figure 2. Schematic diagram of laser cladding principle.

Table 2. Parameters of output power.

Power/W	Scan Velocity/(mm·s^{-1})	Feeding Velocity/(g·min^{-1})	Ar Flow/(L·min^{-1})
900 1200 1500 1800	5	13.5	5

Table 3. Parameters of scanning speed.

Power/W	Scan Velocity/(mm·s^{-1})	Feeding Velocity/(g·min^{-1})	Ar Flow/(L·min^{-1})
1500	3 4 5 6	13.5	5

Table 4. Parameters of overlap.

Overlap Rate	Power/W	Scan Velocity/(mm·s^{-1})	Feeding Velocity/(g·min^{-1})	Ar Flow/(L·min^{-1})
60% 50% 40%	1500	6	13.5	5

2.3. Microstructure Characterization

The sample was cut into a 10 mm × 10 mm × 10 mm metallographic sample using an electric spark wire cutting machine after laser cladding. The section of the cladding layer of the sample was polished and etched with sandpaper and nitric acid alcohol, respectively. The surface of the cladding layer was characterized by the X-ray diffraction (XRD) on a Rigaku D/Max-2400 (Ricoh Group, co., Ltd, Tokyo, Japan) diffractometer with Cu Ka radiation at 40 kV and 200 mA as an X-ray source. The cross-sections were analyzed and characterized by a scanning electron microscope (SEM, JSM-6390A, Japanese electronics (Shanghai) co., LTD, Shanghai, China) equipped with the OXFORD-7718 (Oxford instrument technology (Shanghai) co., LTD, Shanghai, China) energy dispersive spectrometer (EDS).

3. Results and Discussion

The laser cladding layer area was mainly composed of chromium carbide (Cr_3C_2 and Cr_7C_3), as shown in Figure 3a,b. The shapes of the Cr_3C_2 and Cr_7C_3 were dendritic and lath-like or needle-like structures, respectively. NiCr phase was distributed around the chromium carbides. Cr_3C_2 and Cr_7C_3 were hard phases, which can distinctly improve the hardness and wear resistance of the matrix material [35]. NiCr phase was the bonding phase, which was beneficial to improving the toughness of the chromium carbides. In addition, the excellent interface bonding and matching relation of Cr_3C_2 and NiCr were systematically researched in our past work [36]. Therefore, a Cr_3C_2-NiCr laser cladding layer can effectively improve the hardness and wear resistance of the substrate material.

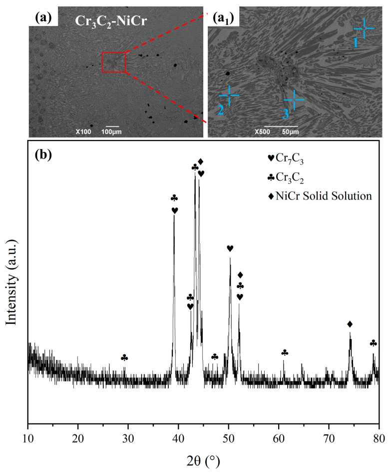

Figure 3. SEM images and XRD diffraction pattern of the surface of laser cladding layer. (**a**) SEM image, (**a$_1$**) Local amplification figure of (**a**), (**b**) XRD diffraction pattern.

The XRD diffraction pattern of the laser cladding layer is shown in Figure 3b. The main phases were Cr_3C_2, Cr_7C_3, and NiCr solid solution. The existence of the NiCr solid solution phase indicated that Ni and Cr elements diffused during the laser cladding. Table 5 shows that the relative values of Cr and C in point 1 and point 2 were 3:2 and 7:3, respectively, which further proved that the main diffraction peaks were Cr_3C_2 and Cr_7C_3. The Cr_7C_3 phase formed mainly because of the slight decarbonization of part of the Cr_3C_2 phase under laser action. The XRD analysis showed that there was no $Cr_{23}C_6$ or oxide phases in the laser cladding layer.

Table 5. Point EDS analysis in Figure 3a_1.

Point	C/(wt. %)	Cr/(wt. %)	Ni/(wt. %)
1	36.76	56.39	6.85
2	22.76	65.00	12.24
3	12.46	46.39	41.15

The schematic diagram of the cross-section of the cladding layer is shown in Figure 4. In this figure, x and h_1 represent the width and height of the cladding layer. The penetration depth of the substrate was marked as h_2. The forming quality of the cladding layer was related to the dilution rate η, which denoted the variation degree of the cladding alloy composition [37]. The computational formula of the dilution rate is shown below.

$$\eta = h_2/(h_1 + h_2) \tag{1}$$

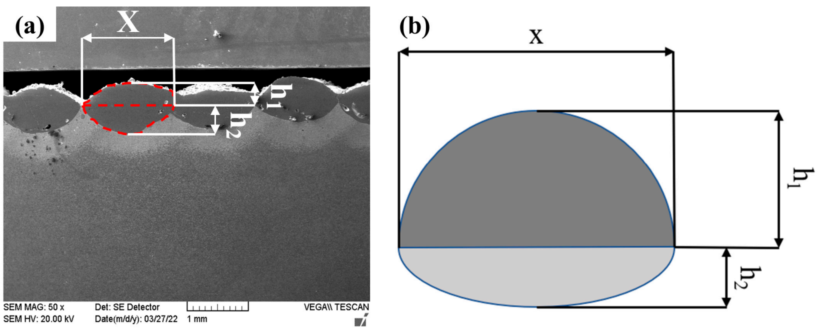

Figure 4. Diagrams of cross-section of cladding layer. (**a**) SEM image, (**b**) schematic diagram.

Figure 5 shows the SEM of the interface structure of Cr_3C_2-NiCr/Q235 steel. The interfacial bonding zone can be roughly divided into the interfacial transition layer, Cr_3C_2-NiCr, and the Q235 steel substrate zone. As shown in Figure 5a–d, tiny cracks were observed on the interface under different output powers. A large number of holes, however, were found in the Cr_3C_2-NiCr region. The reason for these holes was that the powder cannot be fully melted at low power (900 W, 1200 W), while it can be fully melted at high power (1500 W, 1800 W), with fewer holes and a dense cladding layer. The interface was quickly fused with the increase in power and temperature. In addition, the different elements were also rapidly diffused, causing them to react, and resulting in the interface being continuous and smooth. The diffusion coefficient was greater and the movement of atoms was faster at high laser output power and temperature [36]. The transition layer/reaction layer appeared between the Cr_3C_2-NiCr cladding layer and the Q235 steel matrix during the diffusion and reaction of different elements. The formation of the transition layer was beneficial to improving the interface bonding strength. As shown in Figure 5a_1–d_1, the thickness of the interface layer first increased and then decreased as the output power exceeded 1500 W. The thickness of the interface layer of the 1500 W sample was about 50 μm. In comparison, the interface layer was also smoother for the 1500 W sample.

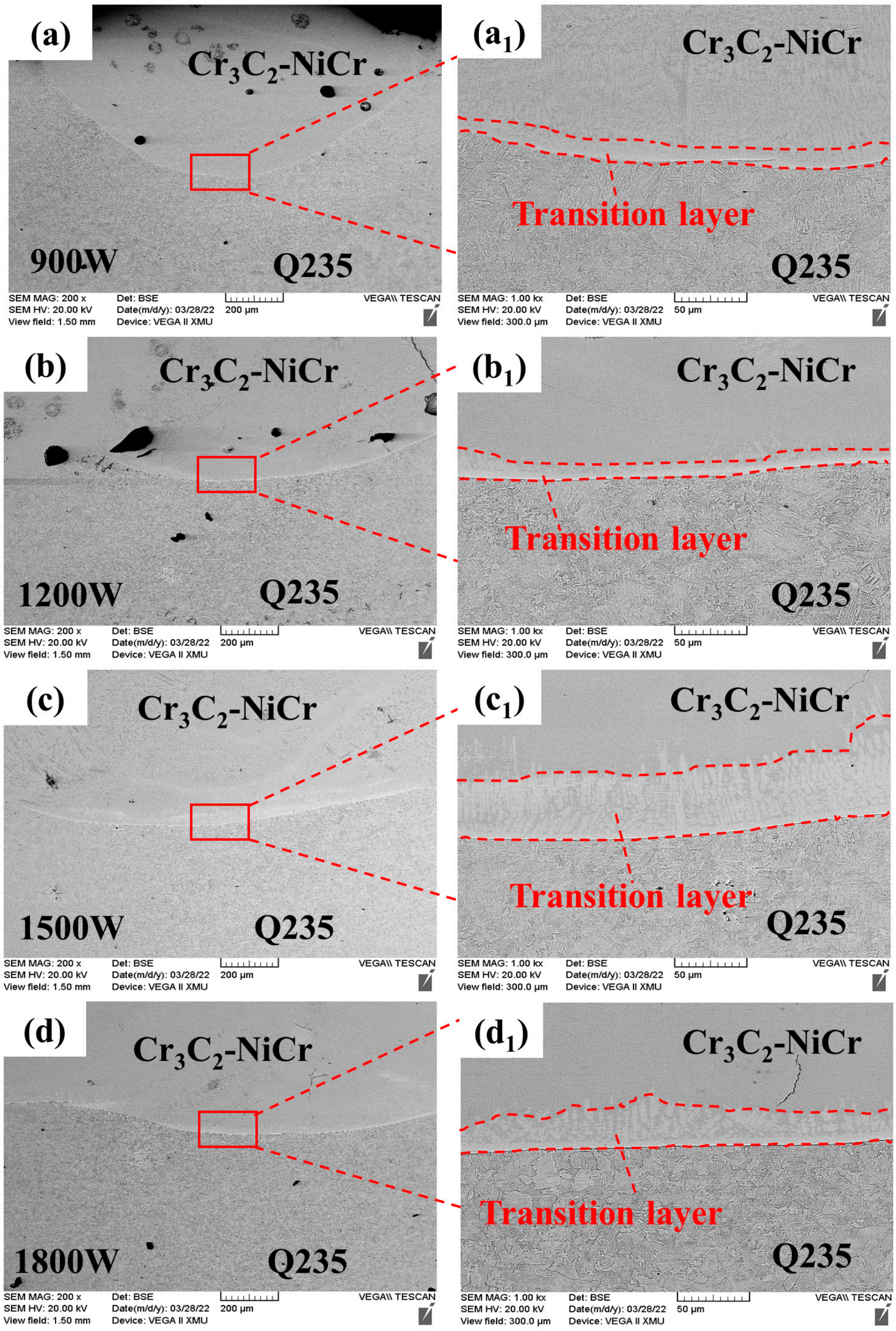

Figure 5. SEM micrograph of the bonding interface of Cr_3C_2-NiCr/Q235 steel with different output power: (**a**) 900 W; (**b**) 1200 W; (**c**) 1500 W; (**d**) 1800 W. (**a_1**) Local amplification figure of (**a**), (**b_1**) Local amplification figure of (**b**), (**c_1**) Local amplification figure of (**c**), (**d_1**) Local amplification figure of (**d**).

Figure 6a,b show the influence of output power on the height and width of the cladding layer. The height and width of the cladding layer increased with the increase in the laser output power. The laser output power had the greater influence on the height of the cladding layer, which was a linear trend. The width of the cladding layer changed slowly as the output power increased from 1500 W to 1800 W. The energy input, temperature, and volume of the molten pool synchronously rose with the increase in output power. The width of the molten pool tended to be stable when the output power increased to a certain range.

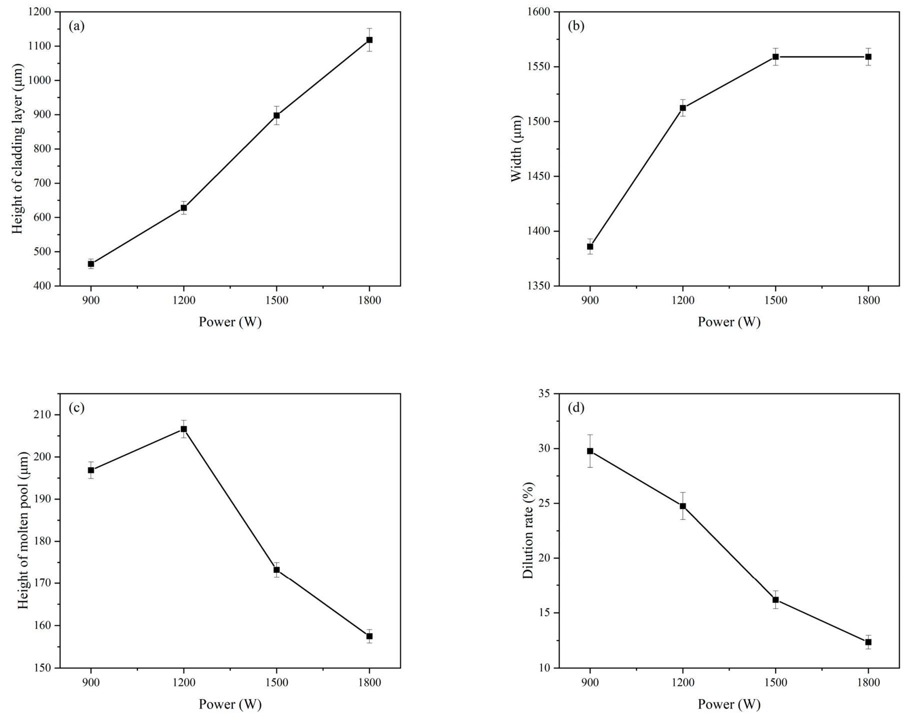

Figure 6. Influence of different output powers on forming quality cladding layer. (**a**) Height of cladding layer; (**b**) width of cladding layer; (**c**) height of molten pool; (**d**) dilution rate.

The depth of the molten pool is exhibited in Figure 6c. The depth of the molten pool increased first, and then decreased with increasing laser output power. In Figure 6c, 1200 W was the highest depth of the molten pool. The output power and temperature were small, at 1200 W, and the energy of the molten pool could not melt the powder evenly. Therefore, the energy mostly accumulated in the molten pool, resulting in the pool's highest depth. The width of the molten pool increased and tended to be stable as the nominal output power increased, along with the increase in output power. The surface tension of the liquid metal decreased, and it could not be balanced due to the gravity in the molten pool. As a result, the liquid metal spread out in the direction of the width, leading to the interface becoming smoother. As shown in Figure 6d, the dilution rate of the coating decreased with the increase in laser output power. The height of the cladding layer increased and the height of the molten pool decreased at the higher output power, leading to the decrease in the dilution rate. Therefore, the forming quality of the cladding layer and the interface became more stable and smoother with the increase in the output power. In addition, the cladding layer and the base material formed an adequate metallurgical combination.

The EDS map scanning of the cladding layer with different laser powers is shown in Figure 7. The main elements detected by surface scanning were Fe, Cr, Ni, and C. The cladding layer was located at the top of the image, which was the enrichment region of Cr and Ni. The Q235 steel was at the bottom, which was the enrichment region of Fe. The diffusion of Fe, Cr, and Ni can be clearly observed in these figures. There was no Fe in the raw material of Cr_3C_2-NiCr; however, Fe can be distinctly seen at the top of the pictures, indicating the existence of element diffusion.

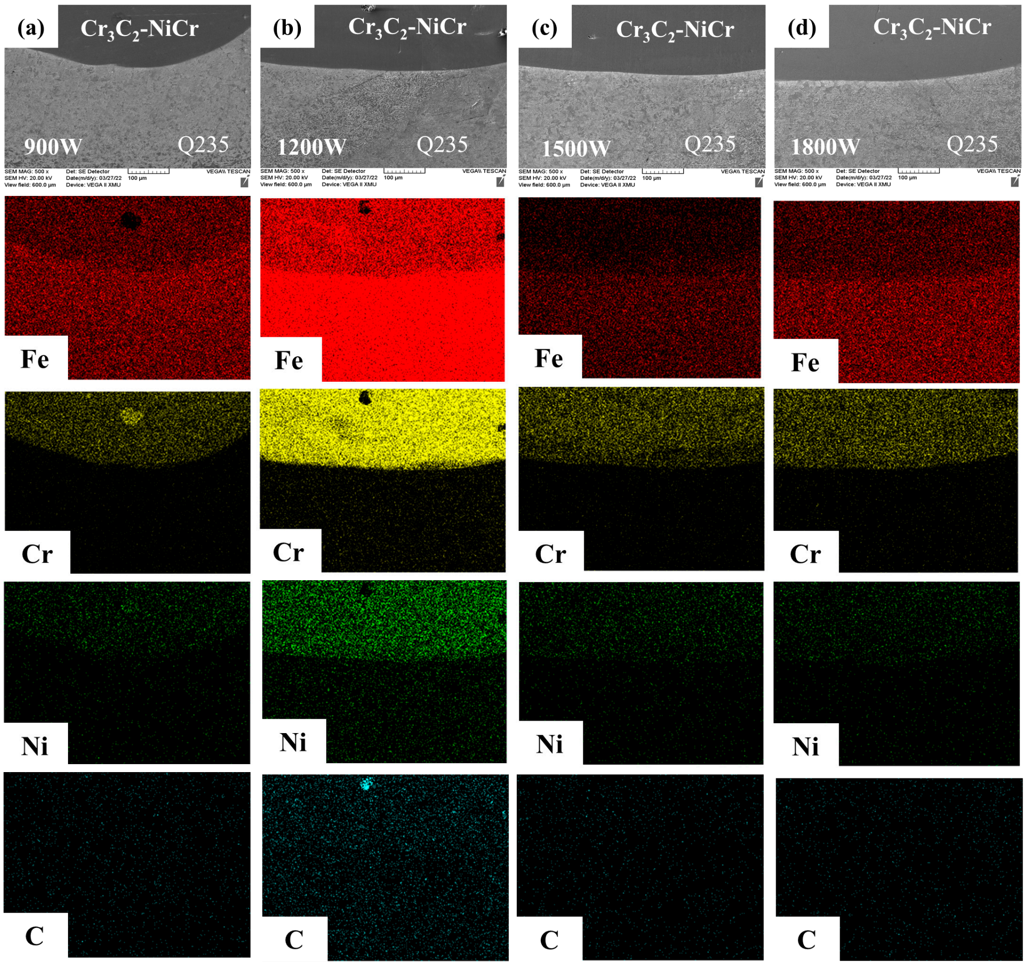

Figure 7. EDS map scanning of the cladding layer with different output powers. (**a**) 900 W, (**b**) 1200 W, (**c**) 1500 W, (**d**) 1800 W.

Figure 8 exhibits the SEM micrograph of the bonding interface of Cr_3C_2-NiCr/Q235 steel with different scanning speeds at 1500 W. The penetration depth became shallower and the weld heat affected zone became narrower, and it was proven that the productivity can be improved with the increase in scanning speed. The alloy powder could not completely melt due to the high cladding speed; however, if the cladding speed was too low, the powder was burned and there was severe loss of the alloying element because of the extended time in the molten pool. At the same time, the heat input of the matrix was large, which increased the deformation of the matrix material. From Figure 8a, a large amount of holes can be seen around the interface between the cladding layer and Q235 steel, mainly because of the lower scanning speed. It is quite clear that the laser cladding quality was adequate for different scanning speeds at 1500 W. The maximum thickness of the transition layer was about 50 μm for the 6 mm/s sample, as shown in Figure 8d_1.

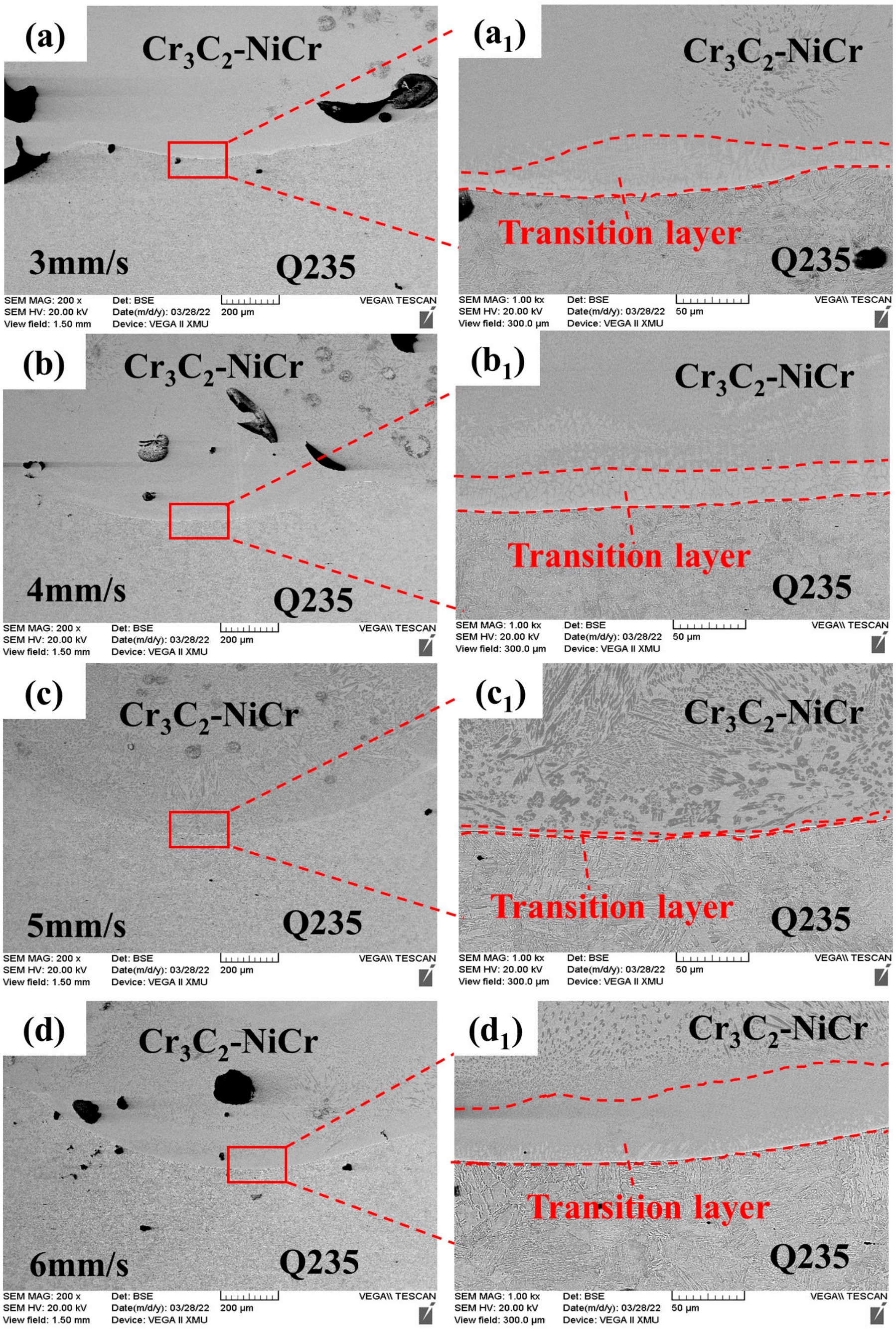

Figure 8. SEM micrograph of the bonding interface of Cr_3C_2-NiCr/Q235 steel with different scanning speeds at 1500 W: (**a**) 3 mm/s; (**b**) 4 mm/s; (**c**) 5 mm/s; and (**d**) 6 mm/s. (**a$_1$**) Local amplification figure of (**a**), (**b$_1$**) Local amplification figure of (**b**), (**c$_1$**) Local amplification figure of (**c**), (**d$_1$**) Local amplification figure of (**d**).

The influence of scanning speed on the height and width of the cladding layer was displayed in Figure 9a,b. The height and width of the cladding layer increased first and then decreased slightly with the increase in the scanning speed. The depth of the molten pool was exhibited in Figure 9c. It was obvious that the depth of the molten pool decreased as the scanning speed increased from 5 mm/s to 6 mm/s. The height of the cladding layer was too thin (about 750 μm) at the low scanning speed (3 mm/s) and the weld heat affected zone was large at a high scanning speed (5 mm/s). Therefore, the weld heat affected zone was smaller and the productivity can be effectively improved for the sample with a 6 mm/s scanning speed. In Figure 9d, the dilution rate of the coating increased first and then decreased slightly with the increase in the scanning speed. The sample with a 6 mm/s scanning speed exhibited the lowest dilution rate.

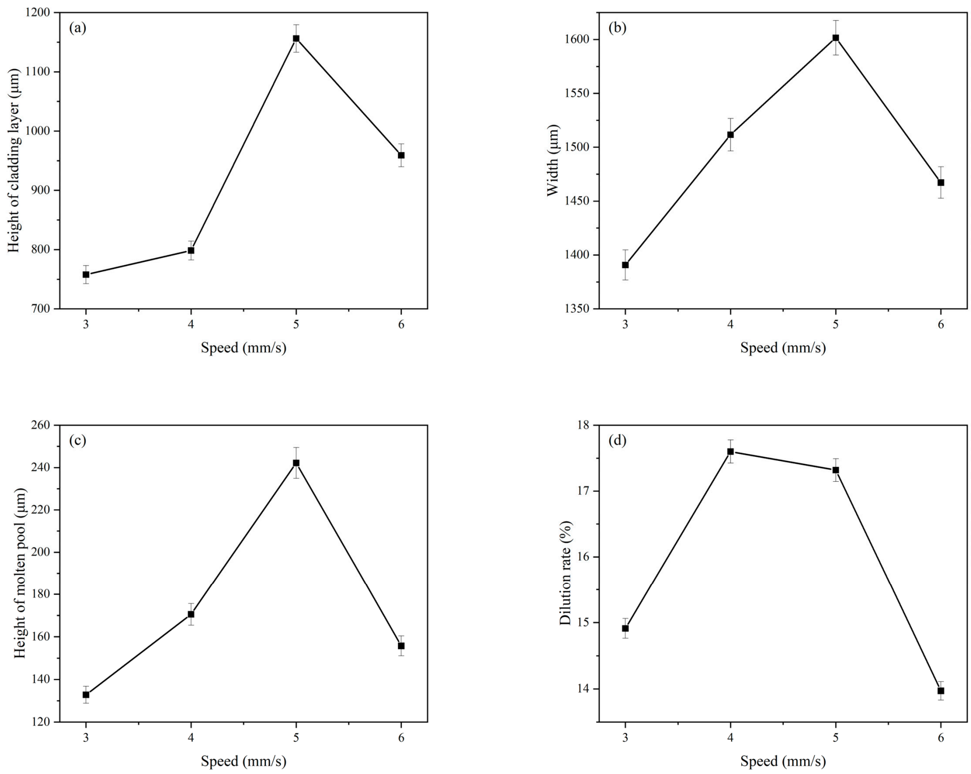

Figure 9. Influence of different scanning speeds on forming quality cladding layer (**a**) Height of cladding layer; (**b**) width of cladding layer; (**c**) height of molten pool; (**d**) dilution rate.

Figure 10 exhibits the SEM micrograph of the bonding interface of Cr_3C_2-NiCr/Q235 steel with a different overlap rate at 1500 W and 6 mm/s. Figure 10a–c show that there were few holes in the SEM micrograph. Overlap rate was the key process parameter, which affected the laser cladding efficiency and flatness. Reducing the overlap rate can improve the laser cladding efficiency to a certain extent; however, it will also lead to the formation of the small gully between the two lap cladding layers, resulting in an uneven laser cladding surface and low flatness. Increasing the overlap rate can improve the flatness of the cladding layer, but it will also reduce the laser cladding efficiency and increase the probability of cracks and porosity defects. It is quite clear that the laser cladding quality was also adequate for different overlap rates at 1500 W and 6 mm/s. The thickness of the transition layer had little change with different overlap rates. The sample with a 40% overlap rate exhibited the best flatness, as shown in Figure 10c_1.

Figure 11 displays the EDS line scanning of the 1500 W, 6 mm/s, and 40% sample. The scanning regions from left to right were the cladding layer, the transition layer, and the Q235 steel substrate, respectively. Iron mainly existed in the steel substrate, which gradually reduced from the transition layer to the cladding layer. On the contrary, Cr and Ni diffused from the cladding layer to the matrix. The maximum thickness of the transition layer was about 50 μm. Fe, Cr, Ni, C, Si, and Mn coexisted in the transition layer region. The diffusion and element reaction occurred in this region, which caused the interface with adequate metallurgical bonding.

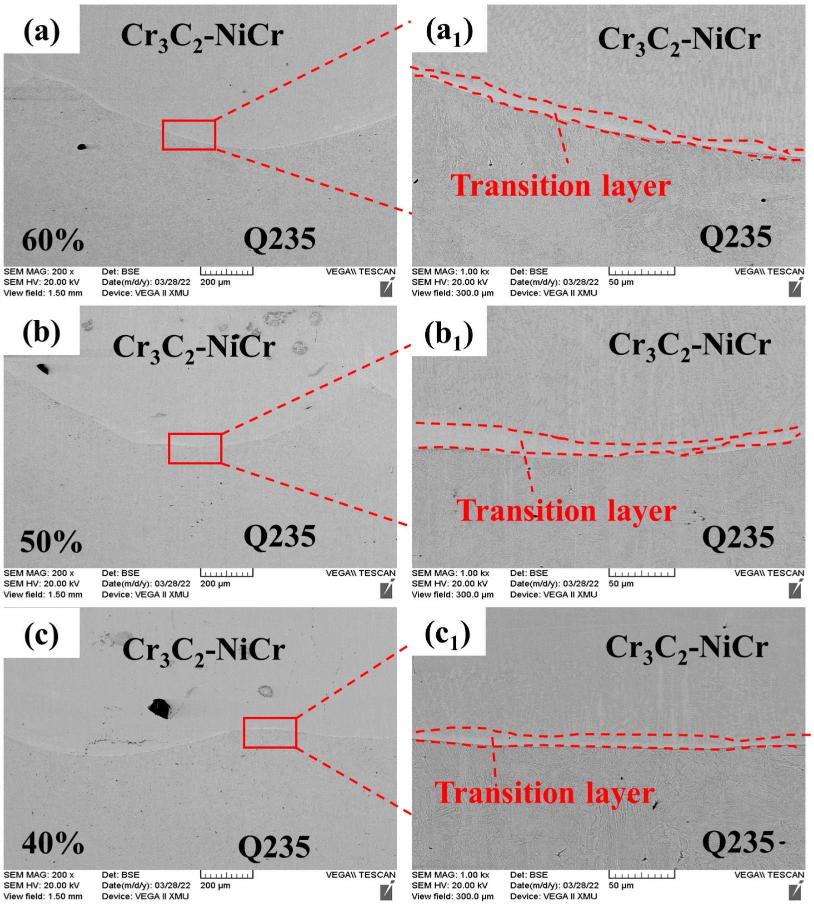

Figure 10. SEM micrograph of the bonding interface of Cr_3C_2-NiCr/Q235 steel with different overlap rate at 1500 W and 6 mm/s: (**a**) 60%; (**b**) 50%; and (**c**) 40%. (**a$_1$**) Local amplification figure of (**a**), (**b$_1$**) Local amplification figure of (**b**), (**c$_1$**) Local amplification figure of (**c**).

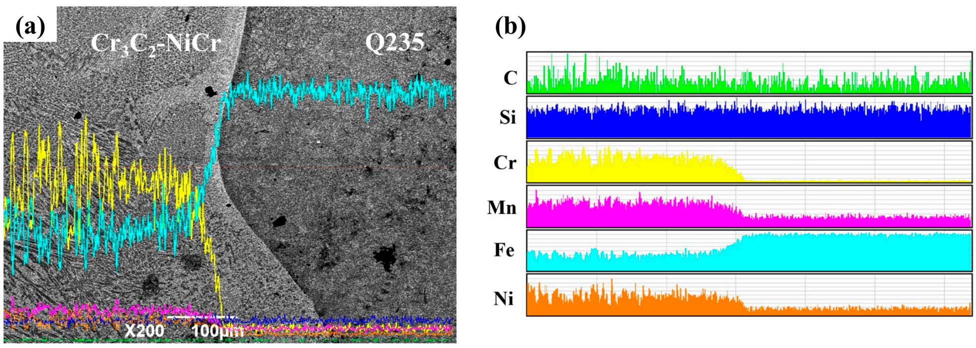

Figure 11. EDS line scanning of the 1500 W, 6 mm/s, and 40% sample. (**a**) SEM image, (**b**) EDS results.

In the EDS line scanning, the diffusion depths of Fe and Cr were deeper than that of Ni, which was due to the larger atomic size. As described in references [38–40], the diffusion rate was related to the atomic size of the alloying elements. According to Fick's law and diffusion dynamics, the mutual diffusion coefficient and atomic vibration energy of alloy elements increases with an increase in temperature. It will also lead to the increase in interatomic diffusion with the increase in output power and temperature, which ultimately improves the bonding quality. Therefore, it can be concluded that the bonding quality of Cr_3C_2-NiCr/Q235 steel increased with the increase in output power and temperature in a certain range.

4. Conclusions

In this paper, the Cr_3C_2-NiCr cermet cladding layer was successfully prepared on the surface of Q235 steel using a high-speed laser cladding method. The effects of laser power, scanning speed, and overlap rate on the microstructure, cladding quality, and interfacial elements diffusion of Cr_3C_2-NiCr/Q235 steel were systematically researched. The conclusions are as follows:

(1) Fe, Cr, and Ni were diffused distinctly between the cladding layer and the matrix. There was an obvious transition layer at the interface of the Cr_3C_2-NiCr cladding layer and Q235 steel, indicating that the Cr_3C_2-NiCr cladding layer had an adequate metallurgical bond with the matrix.

(2) The thickness of the interfacial layer increased and the interface smoothness improved with the increase in the laser power. The maximum thickness of the transition layer was about 50 μm for the 1500 W sample. The maximum thickness of the transition layer was about 50 μm for the 6 mm/s sample, and the weld heat affected zone was smaller and it was proven that the productivity can be effectively improved. The sample with a 40% overlap rate exhibited the best flatness.

(3) The optimal laser power, scanning speed, and overlap rate of the Cr_3C_2-NiCr/Q235 steel were 1500 W, 6 mm/s, and 40%, respectively. These parameters had the interface with adequate metallurgical bonding.

Author Contributions: Conceptualization, W.Z.; Methodology, Y.W.; Software, L.S.; Validation, J.N.; Formal analysis, W.Z.; Resources, S.W.; Writing—original draft, W.Z. All authors have read and agreed to the published version of the manuscript.

Funding: This work was supported by the Natural Science Basic Research Plan in Shaanxi Province of China (2023-JC-YB-458), the Key Research and Development Program of Shaanxi (Program No 2022QCY-LL-58), and the Graduate Student Innovation and Practical Ability Training Program of Xi'an Shiyou University (YCS20211063).

Institutional Review Board Statement: Not applicable.

Informed Consent Statement: Not applicable.

Data Availability Statement: Data sharing is not applicable to this article.

Conflicts of Interest: The authors declare no conflict of interest.

References

1. Glaeser, W.A. Lasers in surface engineering. *Tribol. Int.* **1999**, *32*, 749. [CrossRef]
2. Zhong, M.; Liu, W. Laser surface cladding: The state of the art and challenges. *Proc. Inst. Mech. Eng. Part C J. Mech. Eng. Sci.* **2010**, *224*, 1041–1060. [CrossRef]
3. Vreeling, J.A.; Ocelík, V.; De Hosson, J.T.M. Ti-6Al-4V strengthened by laser melt injection of WC_p particles. *Acta Mater.* **2002**, *50*, 4913–4924. [CrossRef]
4. Majumdar, J.D.; Chandra, B.R.; Mordike, B.L.; Galun, R.; Manna, I. Laser surface engineering of a magnesium alloy with Al+Al_2O_3. *Surf. Coat. Technol.* **2004**, *179*, 297–305. [CrossRef]
5. Sahay, S.S.; Ravichandran, K.S.; Atri, R.; Chen, B.; Rubin, J. Evolution of microstructure and phases in insitu processed Ti-TiB composites containing high volume fractions of TiB whiskers. *J. Mater. Res.* **1999**, *14*, 4214–4223. [CrossRef]
6. Amado, J.M.; Tobar, M.J.; Alvarez, J.C.; Lamas, J.; Yáñez, A. Laser cladding of tungsten carbides (Spherotene®) hardfacing alloys for the mining and mineral industry. *Appl. Surf. Sci.* **2009**, *255*, 5553–5556. [CrossRef]
7. Yang, Y.Q. Microstructure and properties of laser-clad high-temperature wear-resistant alloys. *Appl. Surf. Sci.* **1999**, *140*, 19–23. [CrossRef]
8. Zhou, S.F.; Dai, X.Q. Laser induction hybrid rapid cladding of WC particles reinforced NiCrBSi composite coatings. *Appl. Surf. Sci.* **2010**, *256*, 4708–4714. [CrossRef]
9. Liu, Y.H.; Guo, Z.X.; Yang, Y.; Wang, H.Y.; Hu, J.D.; Li, Y.X.; Chumakov, A.N.; Bosak, N.A. Laser (a pulsed Nd: YAG) cladding of AZ91D magnesium alloy with Al and Al_2O_3 powders. *Appl. Surf. Sci.* **2006**, *4*, 1722–1728. [CrossRef]
10. Wood, R.J.K. Tribo-corrosion of coatings: A Review. *J. Phys. D Appl. Phys. A Europhys. J.* **2007**, *40*, 5502–5521. [CrossRef]
11. Bergmann, C.P.; Vicenzi, J. Protection against erosive wear using thermal sprayed cermet: A Review. In *Protection against Erosive Wear Using Thermal Sprayed Cermet*; Springer: Berlin, Germany, 2011; Volume 1, pp. 1–77.

12. Chang, C.; Verdi, D.; Garrido, M.A.; Ruiz-Hervias, J. Micro-scale mechanical characterization of Inconel cermet coatings deposited by laser cladding. *Bol. Soc. Esp. Ceram. Vidr.* **2016**, *55*, 136–142. [CrossRef]
13. Matthews, S.J.; James, B.J.; Hyland, M.M. Microstructural influence on erosion behaviour of thermal spray coatings. *Mater. Charact.* **2007**, *58*, 59–64. [CrossRef]
14. Lin, L.; Li, G.L.; Wang, H.D.; Kang, J.J.; Xu, Z.L.; Wang, H.J. Structure and wear behavior of NiCr–Cr_3C_2 coatings sprayed by supersonic plasma spraying and high velocity oxy-fuel technologies. *Appl. Surf. Sci.* **2015**, *356*, 383–390. [CrossRef]
15. Gnanasekaran, S.; Padmanaban, G.; Balasubramanian, V.; Kumar, H.; Albert, S.K. Laser hardfacing of colmonoy-5 (Ni-Cr-Si-B-C) powder onto 316LN austenitic stainless steel: Effect of powder feed rate on microstructure. *Mech. Prop. Tribol. Behav.* **2019**, *42*, 283–302.
16. Kathuria, Y.P. Nd-YAG laser cladding of Cr_3C_2 and TiC cermets. *Surf. Coat. Technol.* **2001**, *140*, 195–199. [CrossRef]
17. Wang, K.M.; Fu, H.G.; Liang, Y.P.; Suo, Z.Q.; Pengfei, M. A study of laser cladding NiCrBSi/Mo composite coatings. *Surf. Eng.* **2018**, *34*, 267–275.
18. Betts, J.C. The direct laser deposition of AlSi316 stainless steel and Cr_3C_2 powder. *J. Mater. Process. Technol.* **2009**, *209*, 5229–5238. [CrossRef]
19. Liu, X.B.; Gu, Y.J. Plasma jet clad γ/Cr_7C_3 composite coating on steel. *Mater. Lett.* **2006**, *60*, 577–580. [CrossRef]
20. Jeyaprakash, N.; Yang, C.H.; Duraiselvam, M.; Prabu, G. Microstructure and tribological evolution during laser alloying WC-12%Co and Cr_3C_2-25%NiCr powders on nodular iron surface. *Results Phys.* **2009**, *12*, 1610–1620. [CrossRef]
21. Lou, D.Y.; Yang, K.; Mei, S.; Liu, Q.C.; Cheng, J.; Yang, Q.B.; Liu, D.; He, C.L. The effect of laser scanning speed on microstructure and performance of Cr_3C_2-NiCr cermet fabricated by in-situ laser cladding. *Mater. Sci.* **2021**, *27*, 167–174. [CrossRef]
22. Leo, J.; Lutz-Michael, B.; Jonas, N.; Richard, T.; Sven, T.; Christian, T.; Ville, M.; Petri, V. Improving the high temperature abrasion resistance of thermally sprayed Cr_3C_2-NiCr coatings by WC addition. *Surf. Coat. Technol.* **2018**, *10*, 337.
23. Zhang, D.W.; Lei, T.C.; Li, F.J. Laser cladding of stainless steel with Ni–Cr_3C_2 for improved wear performance. *Wear* **2001**, *251*, 1372–1376. [CrossRef]
24. Venkatesh, L.; Samajdar, I.; Tak, M.; Gundakaram, R.C.; Joshi, S.V. Process parameter impact on microstructure of laser clad inconel-chromium carbide layers. *Mater. Sci. Forum* **2012**, *702–703*, 963–966. [CrossRef]
25. Morimoto, J.; Sasaki, Y.; Fukuhara, S.; Abe, N.; Tukamoto, M. Surface modification of Cr_3C_2-NiCr cermet coatings by direct diode laser. *Vacuum* **2006**, *80*, 1400–1405. [CrossRef]
26. Zhang, D.W.; Lei, T.C. The microstructure and erosive-corrosive wear performance of laser-clad Ni-Cr_3C_2 composite coating. *Wear* **2003**, *255*, 129–133. [CrossRef]
27. Zhang, D.W.; Zhang, X.P. Laser cladding of stainless steel with Ni-Cr_3C_2 and Ni-WC for improving erosive-corrosive wear performance. *Surf. Coat. Technol.* **2005**, *190*, 212–217. [CrossRef]
28. Liu, X.B.; Wang, H.M. Modification of tribology and high-temperature behavior of Ti-48Al-2Cr-2Nb intermetallic alloy by laser cladding. *Appl. Surf. Sci.* **2006**, *252*, 5735–5744. [CrossRef]
29. Rashid, R.R.; Abaspour, S.; Palanisamy, S.; Matthews, N.; Dargusch, M. Metallurgical and geometrical characterisation of the 316L stainless steel clad deposited on a mild steel substrate. *Surf. Coat. Technol.* **2017**, *327*, 174–184. [CrossRef]
30. Barr, C.; Rashid, R.A.R.; Da Sun, S.; Easton, M.; Palanisamy, S.; Orchowski, N.; Matthews, N.; Walker, K.; Brandt, M. Role of deposition strategy and fill depth on the tensile and fatigue performance of 300 M repaired through laser directed energy deposition. *Int. J. Fatigue* **2021**, *146*, 106135. [CrossRef]
31. Rashid, R.A.R.; Nazari, K.A.; Barr, C.; Palanisamy, S.; Orchowski, N.; Matthews, N.; Dargusch, M.S. Effect of laser reheat post-treatment on the microstructural characteristics of laser-cladded ultra-high strength steel. *Surf. Coat. Technol.* **2019**, *372*, 93–102. [CrossRef]
32. Li, G.X.; Rashid, R.A.R.; Ding, S.L.; Sun, S. Machinability Analysis of Finish-Turning Operations for Ti6Al4V Tubes Fabricated by Selective Laser Melting. *Metals* **2022**, *12*, 806. [CrossRef]
33. Venkatesh, L.; Samajdar, I.; Tak, M.; Doherty, R.D.; Gundakaram, R.C.; Prasad, K.S.; Joshi, S.V. Microstructure and phase evolution in laser clad chromium carbide-NiCrMoNb. *Appl. Surf. Sci.* **2015**, *357*, 2391–2401. [CrossRef]
34. Zhai, W.Y.; Gao, Y.M.; Huang, Z.F.; He, L. Cr_3C_2–20%Ni cermets prepared by high energy milling and reactive sintering, and their mechanical properties. *Adv. Appl. Ceram.* **2016**, *115*, 327–332. [CrossRef]
35. Zhai, W.Y. Influence of molybdenum content and load on the tribological behaviors of in-situ Cr_3C_2-20 wt % Ni composites. *J. Alloys Compd.* **2020**, *826*, 154180. [CrossRef]
36. Sun, L.; Hui, W.; Xu, L.; Zhai, W.; Dong, H.; Wang, Y.; He, L.; Peng, J. Interface characterization and mechanical properties of Mo-added chromium carbide-nickel composite. *Ceram. Int.* **2020**, *46*, 27071–27079. [CrossRef]
37. Li, Z.B. Study on Microstructure and Properties of Ni Based Composite Powder Laser Cladding. Master's Thesis, Shandong University, Jinan, China, 2013. (In Chinese).
38. Soria-Biurrun, T.; Lozada-Cabezas, L.; Ibarreta-Lopez, F.; Martinez-Pampliega, R.; Sanchez-Moreno, J.M. Effect of chromium and carbon contents on the sintering of WC-Fe-Ni-Co-Cr multicomponent alloys. *Int. J. Refract. Met. Hard Mater.* **2020**, *92*, 105317. [CrossRef]

39. Wu, Q.L.; Zhang, H.T.Z.Z.H.; Hu, P.; Fan, C.H.; Zhong, N.; Liu, Y. High-temperature wear and cyclic oxidation behavior of (Ti, W) C reinforced stainless steel coating deposited by PTA on a plain carbon steel. *Surf. Coat. Technol.* **2021**, *425*, 127736. [CrossRef]
40. Du, Y.J.; Xiong, J.T.; Jin, F.; Li, S.W.; Yuan, L.; Feng, D.; Shi, J.M.; Li, J.L. Microstructure evolution and mechanical properties of diffusion bonding Al5(TiZrHfNb)$_{95}$ refractory high entropy alloy to Ti_2AlNb alloy. *Mater. Sci. Eng. A* **2021**, *802*, 140610. [CrossRef]